RESEARCH ARTICLE | DECEMBER 08 2025

# A cryogenic uniaxial strain cell for strain-dependent measurements

F. Eckelt ; I. Cavallaro; R. Wagner; A.-A. Haghighirad ; T. Wolf ; J. Wilmers ; S. Bargmann ; C. Hess



*AIP Advances* 15, 125015 (2025)
https://doi.org/10.1063/5.0291096

# A cryogenic uniaxial strain cell for strain-dependent measurements

Cite as: AIP Advances 15, 125015 (2025); doi: 10.1063/5.0291096
Submitted: 15 July 2025 • Accepted: 17 November 2025 •
Published Online: 8 December 2025



F. Eckelt,[1,2,a] I. Cavallaro,[1] R. Wagner,[1] A.-A. Haghighirad,[3] T. Wolf,[3] J. Wilmers,[2,4,5] S. Bargmann,[2,5] and C. Hess[1,2]

## AFFILIATIONS

[1] University of Wuppertal, School of Mathematics and Natural Sciences, 42097 Wuppertal, Germany
[2] Wuppertal Center for Smart Materials, University of Wuppertal, Wuppertal, Germany
[3] Karlsruhe Institute of Technology, Institute for Quantum Materials and Technologies, 76021 Karlsruhe, Germany
[4] Stralsund University of Applied Sciences, Faculty of Mechanical Engineering, 18435 Stralsund, Germany
[5] Chair of Solid Mechanics, School of Mechanical Engineering and Safety Engineering, University of Wuppertal, Wuppertal, Germany

[a] **Author to whom correspondence should be addressed:** eckelt@uni-wuppertal.de

## ABSTRACT

We present the design, implementation, and validation of a cryo-compatible uniaxial strain cell for strain-dependent investigations in quantum materials. The cell is actuated by three large-format piezoelectric stacks and achieves maximum sample displacements of about 38 $\mu$m at room temperature and 1.7 $\mu$m at 5 K. The compact geometry provides an extended mounting area that facilitates the investigation of comparatively large samples and allows flexible contact configurations. The actuators, with a cross-sectional area of $7 \times 7$ mm$^2$, ensure high mechanical stability and enable the application of substantial forces. A key advantage of the design is the high-resolution capacitive displacement sensor, which enables precise *in situ* strain control with excellent temporal resolution, allowing for dynamic strain tracking beyond the capabilities of conventional setups. To operate the strain cell over a broad temperature range from 4.2 to 300 K, a modular measurement probe was developed, allowing efficient thermal coupling and integration into cryogenic environments. The functionality and precision of the setup were demonstrated by elastoresistance measurements on the iron-based superconductor $BaFe_2As_2$ along the [110] direction. The results were compared to those obtained using the conventional approach, in which the sample is directly glued onto a single piezoelectric actuator, showing excellent agreement in amplitude and temperature dependence of the elastoresistance coefficient. Additional tests revealed that the system remains robust under mechanical vibrations introduced by vacuum pumps, enabling stable operation even with liquid nitrogen cooling. Beyond elastoresistivity, the combination of high mechanical stability and time-resolved strain detection makes the presented setup a versatile platform for a broad range of strain-dependent experiments, including future implementations of thermodynamic techniques such as elastocaloric measurements.





## I. INTRODUCTION

Uniaxial pressure represents an effective tuning parameter for selectively modulating the electronic properties of materials. In contrast to hydrostatic pressure, uniaxial stress can directly break the rotational symmetry of a crystal lattice and thereby induce pronounced anisotropies in electronic and structural properties. Prominent examples include $Sr_2RuO_4$, in which uniaxial strain strongly enhances the superconducting transition temperature,[1,2] and $YBa_2Cu_3O_{6.67}$, in which strain along the *a* axis suppresses superconductivity and stabilizes charge order.[3] While such experiments use strain primarily as a tuning parameter to modify material properties, it can also serve as a sensitive probe of how a system responds to symmetry-breaking lattice distortions. This is the basis of elastoresistance measurements, which have emerged as a powerful method to study the coupling between the electronic and lattice degrees of freedom.[4] In these experiments, the change in electrical resistivity is measured as a function of applied uniaxial strain. From such

measurements, one can, for example, extract information about electronic anisotropies and the nematic susceptibility, which has been extensively investigated in Fe-based superconductors, as representative correlated materials.[5–8] A related and more recent approach is elastocaloric measurements, in which the adiabatic temperature or entropy change caused by cyclic strain is detected.[9] This thermodynamic counterpart to elastoresistance provides a sensitive means of identifying strain-induced entropy variations and has been successfully applied to map phase transitions and nematic fluctuations in materials such as $Sr_2RuO_4$ and Fe-based superconductors.[10,11] Because these experiments rely on small, dynamically induced temperature oscillations, they require strain control with high resolution and excellent mechanical stability. Experimentally, various concepts have been realized to apply controlled uniaxial strain, including mechanical spring or screw mechanisms, gas-filled bellows, and bending substrates.[12–18] Compact designs based on piezoelectric actuators enable *in situ* strain control with high precision but can transfer unwanted lateral and thermal deformations to the sample.[6] An elegant and mechanically stable alternative is a strain cell consisting of three piezoelectric actuators.[19] In this design, the actuators vary the distance between two sample mounts, between which the sample is glued, allowing the full actuator stroke to be used to apply substantially larger and more symmetric strains while maintaining excellent mechanical stability. In this work, we present a cryo-compatible uniaxial strain cell optimized for strain-dependent transport investigations. The device features a large mounting area, robust mechanical design, and a high-resolution capacitive displacement sensor that enables time-resolved strain detection. These characteristics make the setup a versatile platform for elastoresistance, elastocaloric, and other strain-dependent measurements, as well as for the further development of advanced strain-based experimental techniques.

## II. MEASUREMENT PROBE

The developed strain cell was designed to be integrated into a custom-built probe assembly. This probe was intentionally constructed as a flexible platform suitable for a variety of low-temperature experiments. It enables precise temperature control in the range from 4.2 to 300 K. For this purpose, it can be inserted into a cryostat or a transport dewar filled with liquid helium, as shown in Fig. 1. The probe is based on a tube design, in which the sample holder is mounted to a flange head via four stainless steel capillaries and inserted into a stainless steel tube with an outer diameter of 49.5 mm. The interior of the probe can be evacuated through the flange head. Thermal contact between the sample holder and the helium bath is established via a cold stage, which is shown in detail in Fig. 2. The cold stage consists of a copper block mounted between the stainless steel capillaries. At this position, a brass tube is soldered into the outer tube. Due to the higher thermal expansion coefficient of brass compared to copper, the brass tube contracts more strongly during cooldown, creating tight mechanical contact with the copper block.[20] This enables efficient thermal coupling between the cold stage and the helium bath. Using this setup, the sample holder can be cooled down to 9 K within ~1250 min [Fig. 3(a)]). By introducing helium exchange gas into the interior of the probe, the cooling process is significantly accelerated, and the base temperature is reduced to ~4.2 K, reducing the total cooling time to just a few hours.

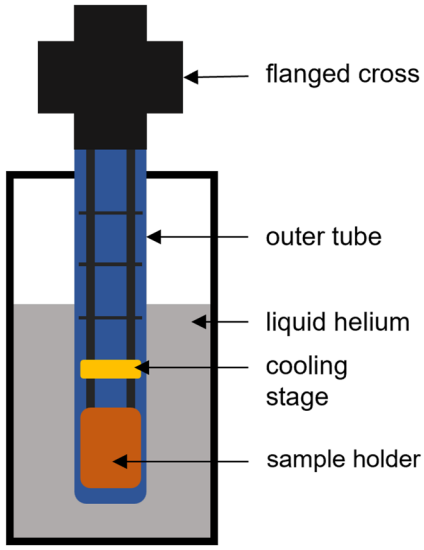


**FIG. 1.** Schematic setup of the experiment. The developed strain cell is mounted onto the sample holder of the custom-designed measurement probe, which is enclosed within a stainless steel tube and can be evacuated via the flange head. Thermal contact to the cryogen is established through a cold stage.

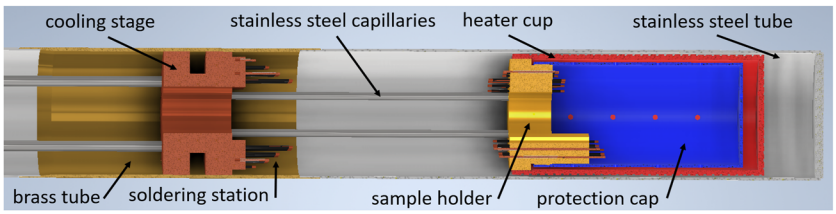


**FIG. 2.** Lower end of the probe. At the bottom of the probe, the sample holder is mounted to four stainless steel capillaries, which are connected to the probe's flange head. For temperature control, a protective cap and a heater cup made of gold-plated copper can be screwed onto the sample holder. A total of 28 electrical connections are available at the sample holder, eight of which are used for temperature measurements using a Cernox 1050-SD-HT and a Pt100 sensor. Thermal contact to the helium bath is established via a copper cold stage, which is thermally anchored to the outer stainless steel tube through a soldered-in brass sleeve. To minimize thermal load from the measurement wires, they are thermally anchored at the cold stage via a soldering platform and routed in pairs through fabric sleeves inside the capillaries for mechanical and thermal protection.

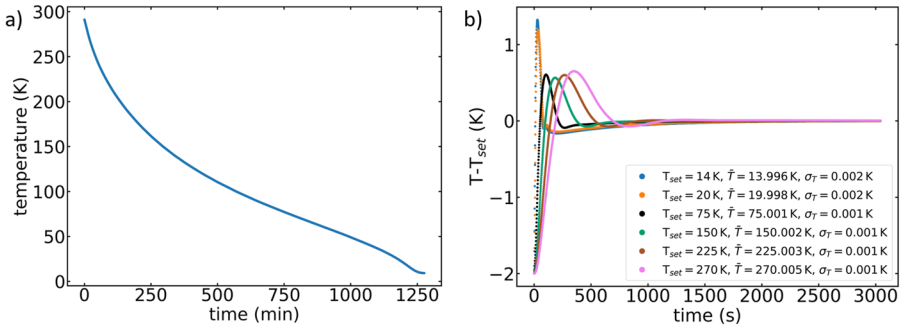


**FIG. 3.** (a) Cooldown curve of the probe using liquid helium. The base temperature of 9 K is reached after ~1250 min. The cooldown process can be significantly accelerated by introducing helium exchange gas into the interior of the probe. (b) Temperature regulation of the sample for various target temperatures. To allow for better comparison, the difference between the actual sample temperature and the setpoint is plotted. The legend includes the mean temperature ($\bar{T}$) and standard deviation ($\sigma_T$) in the time interval between 2000 and 3000 s after the setpoint change.

The sample holder is equipped with a total of 28 electrical contacts. Two groups of four contacts each are dedicated to four-point resistance measurements using a Cernox 1050-SD-HT sensor (Quantum Design, USA) and a Pt100 sensor (Testo SE & Co. KGaA, Germany) for temperature monitoring. Electrical connections are made using 50 $\mu$m thick copper wires running from the sample holder to the flange head. To minimize the thermal load on the sample, these wires are thermally anchored to the cold stage via a soldering platform. From there, they continue to the flange head, routed through fabric sleeves inside the stainless steel capillaries for mechanical stabilization. For ease of use in four-point resistance measurements, the wires are grouped in sets of four and connected to vacuum feedthroughs at the top of the probe, which likewise support four-wire connections. To reduce electromagnetic interference, the measurement lines are twisted in pairs. Temperature control is achieved via a heater cup made of gold-plated copper, which can be mounted onto the sample holder. The outer surface of the heater contains a double spiral into which two parallel-connected, 100 $\mu$m thick manganin wires are glued. These wires have a total length of ~2 m and a combined resistance of 170 Ω. To shield the sample from direct thermal radiation emitted by the heater, an additional protective cap made of gold-plated copper is installed over the sample holder [Fig. 3(a)]. The screw-on thermal radiation shield defines a usable mounting area of 34 × 90 mm$^2$ (width × length). The maximum usable height is limited by the circular cross-section and reaches up to ~25 mm, depending on the width of the sample. A Lakeshore 340 temperature controller (Lake Shore Cryotronics) is used for temperature regulation. It provides a maximum output power of 100 W at up to 50 V and 2 A. The power is regulated via an internal PID controller that adjusts the output voltage. Given the heater resistance of 170 Ω, the maximum achievable heating power is ~14 W.

Figure 3(b) shows the temperature regulation performance for various setpoints. For better comparison, the difference between the measured sample temperature and the target temperature is plotted over time. The data demonstrate that the target temperature can be precisely reached across the entire temperature range. A small overshoot is observed at the beginning of each regulation cycle, with its magnitude slightly depending on the setpoint. To evaluate the stability, the temperature mean value $\bar{T}$ and standard deviation $\sigma_T$ are indicated in the legend for the interval between 2000 and 3000 s after the setpoint change. The largest deviation of the mean temperature from the setpoint was only 5 mK at 270 K. The highest observed standard deviation was just 2 mK at 14 and 20 K, highlighting the high quality of the temperature control system.

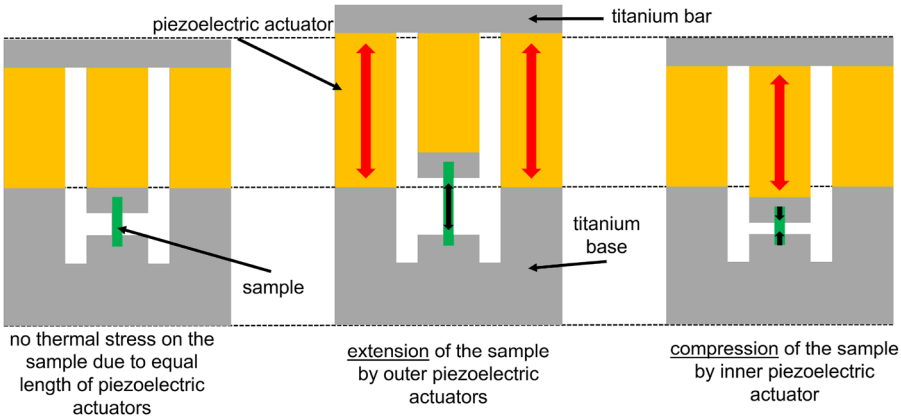


**FIG. 4.** Operating principle of the strain cell. The use of three piezoelectric actuators of equal length ensures compensation of thermal expansion, allowing for strain-free cooling of the sample. Tensile strain is applied by extending the two outer actuators (center), while compressive strain is induced by extending the central actuator (right).

## III. STRAIN CELL

The strain cell is based on a concept by Hicks *et al.*[19] and essentially consists of three piezoelectric actuators that generate the mechanical load on the sample. The setup and working principle of this approach are illustrated in Fig. 4. The sample (green) is mounted between two sample mounts, which can be displaced relative to each other by means of the three piezo actuators (orange). When the two outer actuators are extended, a tensile strain is applied to the sample (center). Conversely, extending the central actuator compresses the sample (right). Since all three piezo actuators are of equal length, their thermal expansion compensates during cooldown, allowing the sample to reach cryogenic temperatures without mechanical stress. Figure 5 shows a top view of the lower part of the strain cell. The sample plates are used to mount both ends of the sample. The distance between these plates determines the maximum achievable strain according to $\varepsilon = \Delta L/L_0$, where $\Delta L$ is the displacement generated by the piezo actuators and $L_0$ is the initial distance between the sample plates in the unloaded state. By varying the length of the plates, $L_0$ and, thus, the maximum achievable strain can be adjusted. The maximum distance between the sample mounts is 4 mm. The strain cell can be mounted to the probe via the mounting holes.

To stabilize the motion of the movable sample mounts against rotational and lateral displacement, and to protect the central piezo actuator from unintended lateral forces, for example, during sample mounting, it is connected to the titanium base via four bending elements. Due to their geometry, these elements exhibit a low spring constant for axial motion, while providing significantly higher stiffness against rotational or transverse movements.

### A. Finite element analysis

To verify the mechanical behavior of the bending elements and determine the thickness $d$ and radii $R_i$ and $R_a$ at the junctions with the rest of the strain cell (see Fig. 6), a finite element analysis was conducted using Abaqus CAE. A mesh composed of hexahedral elements with eight nodes, reduced integration (C3D8R), and hourglassing control was employed. This choice of elements provides a good balance between computational effort and accuracy, particularly for three-dimensional structures. The material, assumed to be linear elastic, was titanium grade 2 with Young's modulus of 103 MPa and Poisson's ratio of 0.33.[21]

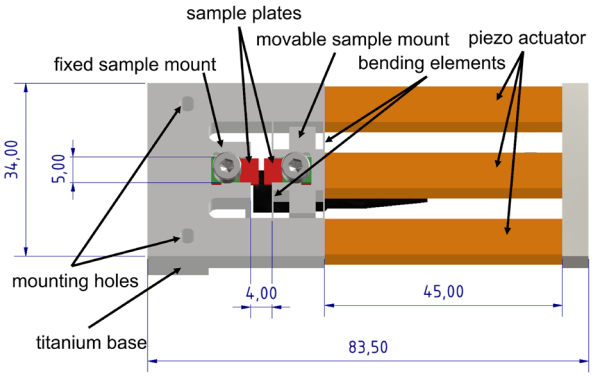


**FIG. 5.** Top view of the titanium base section of the strain cell.

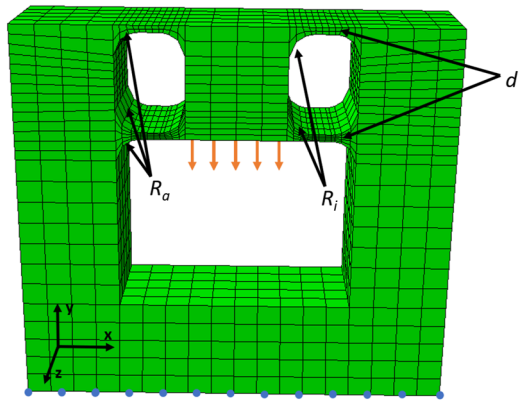


**FIG. 6.** Structured mesh applied to the entire geometry of the component. The mesh is locally refined in critical areas, especially where the bending elements connect to the top of the cell, to ensure greater accuracy in areas of expected higher stress or strain. The bottom of the component is fixed for the simulation, as indicated by the blue points. The force is applied to the movable sample mount, as shown by the orange arrows.

A structured mesh was used (see Fig. 6). In regions of particular interest, where higher stresses or strains were expected, the mesh was locally refined. This specifically applies to the upper part of the cell, where the bending elements are connected to the rest of the component. This refinement ensures that the stress distribution in these critical areas is accurately captured.

To accurately replicate the function of the cell in the simulation, the load on the component was applied by displacing the movable sample mount, as depicted in Fig. 6. The orange arrows illustrate the applied displacement direction. A displacement of 50 $\mu$m was used for the calculations. The lower part of the component was fixed, indicated by the blue points. Figure 7 shows a representative von Mises stress map for an imposed displacement of 50 $\mu$m applied to the movable sample mount. It clearly illustrates that the transition regions with radii are subject to particularly high mechanical loads. This increased stress in the transition areas is the reason why both the radii and the thickness were systematically varied in the simulations. To assess the load within the component, the von Mises stress

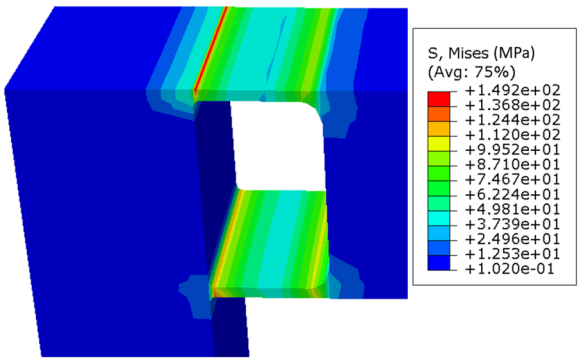


**FIG. 7.** Color-coded visualization of the von Mises stress distribution on the component. The maximum stress occurs in the radii of the bending elements.

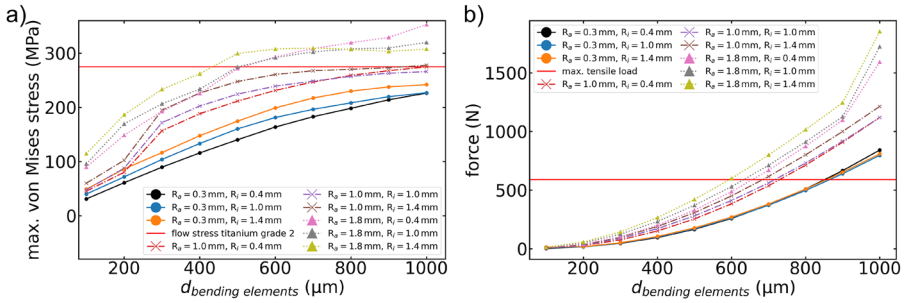


**FIG. 8.** (a) Simulation results showing the maximum von Mises stress for various combinations of inner and outer radii $R_i$ and $R_a$ plotted as a function of the thickness $d$, which corresponds to the thickness of the bending elements. The maximum allowable stress for titanium grade 2 is indicated in red. (b) Required force for a displacement as a function of thickness $d$, inner radius $R_i$, and outer radius $R_a$. The maximum tensile force that a piezo stack can withstand is indicated in red.

was utilized. This stress measurement combines the effects of normal and shear stresses into a single quantity, providing a conservative estimate of material failure. The calculated von Mises equivalent stress was compared to the yield strength of titanium grade 2, which is 275 MPa.[21] In Fig. 8(a), the simulation results for different geometries are depicted, showing various combinations of inner and outer radii plotted vs the thickness $d$. The output stress value is the maximum von Mises stress from all elements. Both larger inner and outer radii $R_i$ and $R_a$, as well as greater thicknesses $d$, lead to higher stresses in the component. The yield strength of titanium grade 2, which is 275 MPa, is marked in red for comparison. For most configurations, the stresses in the component do not reach the yield strength, indicating that the bending elements deform only elastically. In Fig. 8(b), the force required to displace the movable sample mount is shown for the same geometric configurations as in Fig. 8(a). The plotted values represent the force required to achieve a displacement of 50 $\mu$m for various combinations of inner and outer radii $R_i$ and $R_a$, as a function of thickness $d$. The required force increases slightly with increasing inner and outer radii and shows a quadratic dependence on thickness. The piezoelectric actuators used in this setup are made of sintered ceramic layers and are, therefore, sensitive to tensile stress. During both tensile and compressive loading of the sample, at least one actuator is always subjected to tensile force. In a uniaxial tensile test performed on one of these actuators, mechanical failure occurred at a load of 590 N. To ensure a sufficient safety margin, the maximum operational load should remain well below this value. For comparison, this maximum load is indicated by the red line in Fig. 8(b). Here, it should be noted that the load applied during the experiment must also cover the force required to deform the specimen itself. The simulation results show that small transition radii $R_i$ and $R_a$ are desirable, as they reduce both mechanical stress in the component and the required actuation force. In practice, the minimum achievable radii are limited by manufacturing constraints. Using wire electrical discharge machining, a minimum radius of 0.3 mm can be achieved, which is sufficient to allow for a suitable component configuration. For $R_i = R_a = 0.3$ mm, the von Mises stresses remain within the elastic range for all simulated thicknesses [see Fig. 8(a)]. The required force also remains within the performance limits of the actuators for thicknesses up to 900 $\mu$m [see Fig. 8(b)]. A thickness of 400 $\mu$m was chosen to achieve a balance between high force reserves and minimal stress on the piezo stacks, as confirmed by simulation. It should be noted that during the operation of the strain cell, at least one piezoelectric actuator is always under tensile load, which can reduce its lifetime and, in the worst case, lead to failure. The actuators are bonded into the strain cell using Staycast 2850FT, such that, in the event of a defect, the damaged actuator can be removed and replaced by gluing in a new one. Owing to the modular design of the strain cell, the actuators can be regarded as exchangeable components that can be easily exchanged.

## B. Strain measurement

The distance between the sample mounts is monitored with a capacitive displacement sensor (model CSH05; Micro-Epsilon, Germany). The sensor provides a measurement range of 1 mm and allows for a maximum temporal resolution of up to 8.5 kHz, at which it achieves a resolution of 10 nm.[22] The operating principle is based on an ideal parallel-plate capacitor, where the sensor and an opposing target form the two capacitor plates. The sensor is mounted in a holder on the underside of the strain cell and is attached to the movable sample mount, while the sensor target is a titanium reflector that forms part of the fixed sample mount. For accurate operation, the target must be electrically grounded to ensure a stable electric potential and to shield the measurement signal from electrical noise and static charge accumulation. The underside of the strain cell, including labeled components, is shown in Fig. 9.

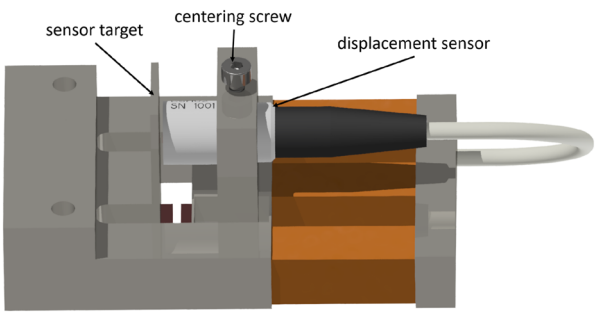


**FIG. 9.** Lower part of the strain cell with the capacitive displacement sensor, which can be mounted to the movable sample mount using a centering screw. The sensor measures the distance to the fixed sample mount via a sensor target.

### C. Influence of vacuum pumps

During measurements in liquid nitrogen, the reduced cryopumping effect compared to liquid helium leads to a noticeable degradation of the vacuum inside the probe despite the low leak rate of the setup ($1.55 \times 10^{-5}$ mbar l/s). As a result, thermal coupling is enhanced, and the available heating power of 14 W is no longer sufficient to raise the sample temperature to room temperature. This issue can be resolved by evacuating the probe with a vacuum pump. To investigate the influence of vacuum pumping on the measurement, both a scroll pump and a turbomolecular pump were tested. The pumps were connected to the probe via a flexible metal hose. Figure 10(a) shows the distance measurement under different pumping configurations, revealing no significant impact on the displacement signal. In addition, measurements of the strain-dependent change in the electrical resistance were carried out on $BaFe_2As_2$ at 138 K [see Fig. 10(b)] using the same pump configurations, as shown in Fig. 10(a). Again, no substantial influence on the data was observed. These results demonstrate that the probe can reliably be used with liquid nitrogen for extended elastoresistance measurements, without compromising the ability to heat the sample to high temperatures. Furthermore, they highlight the robustness of the developed strain cell against minor vibrations transmitted through the vacuum hose from the pumps.

### D. Maximum displacement

In the final version of the strain cell, three piezoelectric actuators model PST 150/7 × 7/50 from Piezomechanik GmbH, Germany, each 45 mm long and with a cross-section of 7 × 7 $mm^2$, were installed. This results in overall dimensions of the strain cell of 22 mm (height) × 83.5 mm (length) × 34 mm (width). To characterize the performance, the distance between the sample mounts was measured as a function of the applied piezo voltage at different temperatures. The resulting maximum displacement is shown in Fig. 11, which demonstrates a pronounced temperature dependence. At 5 K, the maximum displacement amounts to about 1.7 $\mu$m, while at room temperature, it reaches about 38 $\mu$m. This large displacement range allows a significant strain to be applied to the sample, although the actual strain achieved depends on the sample length.

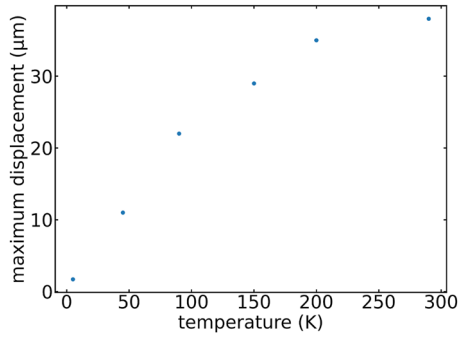


**FIG. 11.** Maximum displacement of the sample mounts as a function of temperature.

### E. Test measurements

To validate the functionality of the developed strain cell, elastoresistance measurements were performed on a single-crystalline $BaFe_2As_2$ sample along the [110] direction and compared to results obtained using the conventional method, in which the sample is glued directly onto a piezoelectric actuator, and the strain is monitored using a surface-mounted strain gauge.[6,7] In the absence of external strain, $BaFe_2As_2$ undergoes an antiferromagnetic phase transition at ~138 K, which is accompanied by a structural distortion that breaks the fourfold symmetry of the high-temperature tetragonal phase.[23–25] This orthorhombic distortion is relatively small and is driven by an electronically induced nematic instability. The electronic origin of the symmetry breaking manifests itself in a pronounced in-plane resistivity anisotropy. The strong coupling between the electronic anisotropy and the lattice makes $BaFe_2As_2$ an ideal test material for strain experiments. In particular, the [110] direction is highly sensitive to uniaxial strain, as it selectively couples to the nematic order parameter.[4,5,15]

For the measurement, a piece of the crystal was cut into a rectangular shape along the [110] direction, resulting in final sample dimensions of 3 mm × 0.5 mm × 50 $\mu$m. The distance between the sample plates was set to 1.5 mm, and the sample was glued using Stycast 2850FT. Electrical contacts were made using four 50 $\mu$m thick

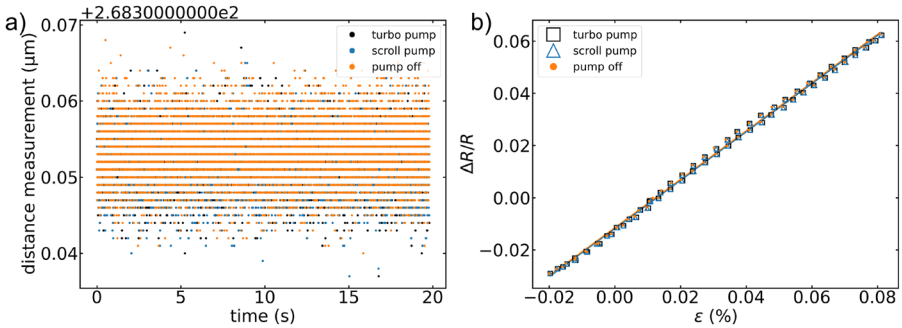


**FIG. 10.** Investigation of the influence of vacuum pumps on the measurement. (a) Time-resolved measurements of the gap between the sample mounts at a fixed setpoint distance for different pump configurations (none, scroll pump, turbomolecular pump) show no significant effect on the signal. (b) Strain-dependent resistance change measured at 138 K on a test sample of $BaFe_2As_2$ under the same pump configurations, also showing no measurable influence from the pumps. The individual data points are barely visible, as they lie almost entirely on top of each other.

silver wires attached with Hans Wolbring conductive silver 200 N. For each measurement, the sample temperature was stabilized and the strain was varied continuously between −0.1% and +0.1% by adjusting the applied piezo voltage in steps of 1 V. The resistance was always measured after the piezo voltage had been changed, and an additional waiting time was introduced after each adjustment in order to minimize creep effects of the piezo actuators. To suppress thermoelectric offsets and ensure reliable values, the polarity of the applied current was alternated for each data point. A program flow diagram of the elastoresistance measurements is shown in Fig. 12. Figure 13(a) shows the strain-dependent relative resistance change $(R - R_0)/R_0$, where $R_0$ is the resistance of the unstrained sample. At all temperatures, a linear relationship between resistance change and strain is observed. At low temperatures, the noise level increases slightly due to the lower sample resistance. The elastoresistance coefficient $\tilde{n}$ is defined as the slope of the linear dependence of the relative resistance change in strain. The temperature dependence of $\tilde{n}$ is shown in Fig. 13(b) and exhibits the expected increase upon cooling, followed by a decrease above the nematic transition temperature $T_{\mathrm{nem}}$. Above $T$ = 139 K, the data can be described by a Curie–Weiss-like behavior of the following form:

$$\tilde{n} = n_0 + \frac{\lambda/a_0}{T - T_{\mathrm{nem}}}, \tag{1}$$

as indicated by the green line in Fig. 13(b).[26] To confirm the measurement results, an additional elastoresistance experiment on $BaFe_2As_2$ was performed using the conventional method, in which the sample is directly glued onto a piezoelectric actuator. The result is shown in Fig. 14(a), together with the previously presented measurement using the developed strain cell. In this reference measurement, the expected divergent temperature dependence is again observed and can also be described by a Curie–Weiss-like behavior. A high degree of agreement is found between the two datasets. In particular, the matching amplitude of the elastoresistance signals confirms that the strain in the developed strain cell is correctly determined. Notably, the measurement using the strain cell exhibits significantly lower noise compared to the conventional method. This may be attributed to less effective strain transfer in the conventional setup. To further assess the reliability of the measurement approach using the strain cell, a second elastoresistance experiment was conducted, but this time using liquid nitrogen as the cryogenic medium. The results are shown in Fig. 14(b), together with the original measurement. Both measurements exhibit a high degree of agreement. The small deviations observed can likely be attributed to the slight misalignment of the samples during mounting. The fit parameters extracted from the different measurements are summarized in Table I. These results further confirm the good agreement between the different measurement approaches. The parameter $\lambda/a_0$ serves as a measure of the strength of nematic fluctuations. The largest deviation is observed between the measurement of sample

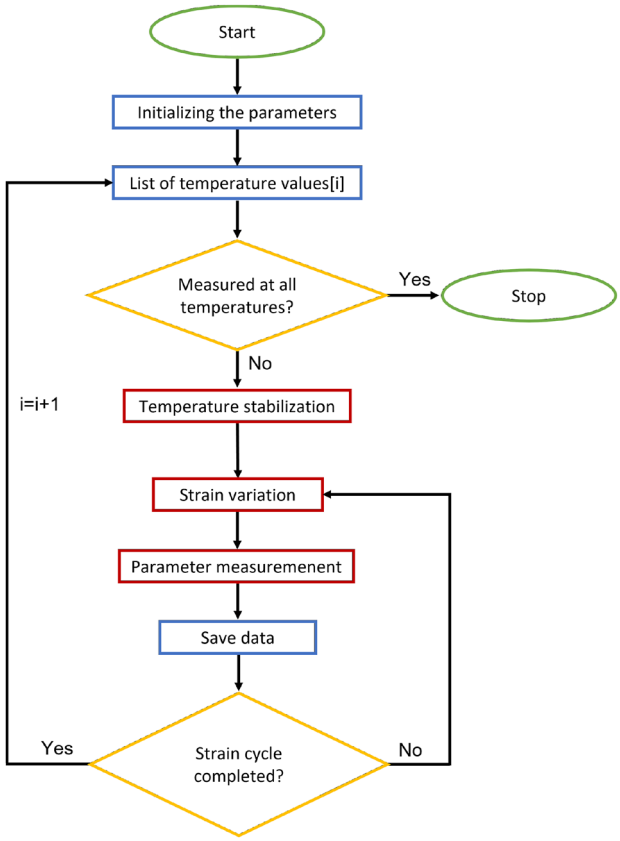


**FIG. 12.** Program flow diagram of the elastoresistance measurement. After the initialization of the measurement parameters, the sample temperature is stabilized. For each temperature, the selected strain cycle is performed while the sample resistance and strain are measured. Once the cycle is completed, the next temperature is stabilized, and the strain is varied again. This procedure is repeated until all temperature steps have been measured.

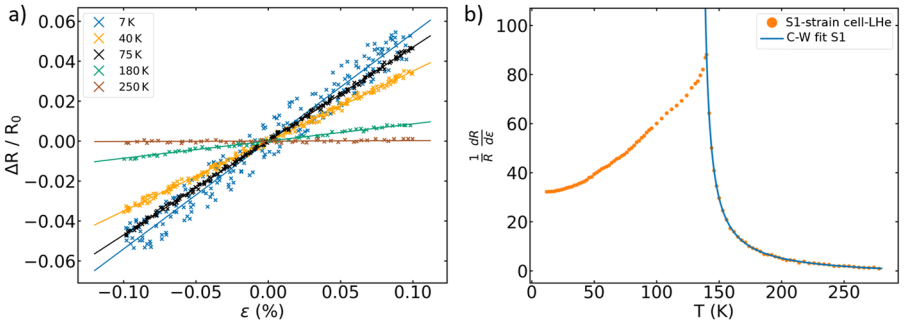


**FIG. 13.** (a) Strain-dependent relative resistance change in S1 (S1-strain cell-LHe) measured with the strain cell at various temperatures. (b) Temperature dependence of the elastoresistance coefficient of sample 1 with Curie–Weiss fit.

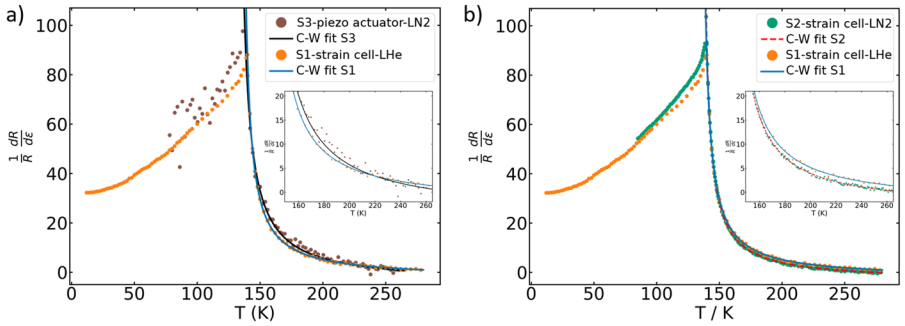


**FIG. 14.** Comparison of the elastoresistance measurement of S1 (S1-strain cell-LHe) with (a) an additional measurement performed using the conventional method, where the sample is directly glued onto the surface of the piezoelectric actuator (S3-piezo actuator-LN2), and (b) a further elastoresistance measurement using the strain cell with liquid helium cooling (S2-strain cell-LHe). In both panels, the temperature range between 150 and 260 K is shown enlarged in an inset to facilitate comparison.

**TABLE I.** Fit parameters from the Curie–Weiss fits to the elastoresistance measurements of $BaFe_2As_2$. The labels indicate the sample (S1–S3), the measurement method (strain cell or piezo actuator), and the cooling medium (LN2 or LHe).

| Measurement method | $\lambda/a_0$ (K) | $T_{nem}$ (K) | $n_0$ |
|---|---|---|---|
| S1-strain cell-LHe | 481 ± 3 | 135.43 ± 0.01 | 3.46 ± 0.04 |
| S2-strain cell-LN2 | 499 ± 4 | 134.73 ± 0.04 | 2.47 ± 0.06 |
| S3-piezo actuator-LN2 | 521 ± 29 | 131.9 ± 0.4 | 4.1 ± 0.4 |

1 using the strain cell and the one obtained via the conventional method, but this deviation amounts to only 8%. In contrast, the two measurements performed with the strain cell show excellent agreement, with a relative deviation of only 3.6% in $\lambda/a_0$. The transition temperature $T_{nem}$ also shows the largest discrepancy between the strain cell and the conventional measurement, with a relative deviation of just 2.5%. Between the two strain cell measurements, the relative deviation in $T_{nem}$ is only 0.5%, further highlighting the reproducibility of the results. The fact that all extracted values for $T_{nem}$ lie below the known transition temperature of $T_{nem,lit}$ = 138 K is attributed to the coupling between the electronic nematic order and the crystal lattice.[5] The parameter $n_0$ reflects the intrinsic piezoresistive background and is not related to the electronic nematicity. Here, as well, only minor variations are observed across the different measurement approaches.

## IV. SUMMARY

In this work, we presented the construction of a cryo-compatible uniaxial strain cell based on three piezoelectric actuators. The device was developed for strain-dependent transport measurements. At room temperature, the maximum sample displacement reached 38 $\mu$m, while at 5 K, a displacement of 1.7 $\mu$m was achieved. The displacement was monitored with high precision using a capacitive sensor providing excellent temporal resolution. Compared with conventional designs, the strain cell described here offers several advantages. The large-format piezoelectric actuators with a cross-sectional area of $7 \times 7$ mm$^2$ ensure outstanding mechanical stability. In addition, the geometry of the device provides an extended mounting area that facilitates convenient sample placement and flexible contact configuration. The high time resolution of the displacement sensor further enables dynamic strain tracking, which is not possible with standard strain-cell setups. To enable measurements at low temperatures, a modular probe was developed into which the strain cell can be integrated. The probe is designed for cooling with liquid helium down to 4.2 K. With an outer diameter of 49.5 mm, the probe is compact enough to fit into cryostats with a clear inner opening of 50 mm, thereby allowing, in principle, measurements under an external magnetic field. The functionality of the entire system was demonstrated by elastoresistance measurements on $BaFe_2As_2$. The results were consistent with those obtained using the conventional method, where the sample is glued directly onto a single piezo actuator, but showed significantly improved data quality when using the newly developed strain cell. Furthermore, the mechanical stability of the setup was confirmed by simultaneous operation of vacuum pumps, which did not have a significant effect on the measurement results. Beyond elastoresistivity, the strain cell provides a versatile platform for other strain-dependent measurements. In particular, its combination of high mechanical stability and time-resolved strain detection could be advantageous for techniques such as elastocaloric experiments, which require precise and dynamic strain control. These features make the presented design a promising foundation for the further development of advanced strain-based experimental methods.

## ACKNOWLEDGMENTS

The authors would like to thank Frederic Braun, Lukas Voss, and Florian Brockner for their assistance in setting up the experiment and for the many insightful discussions that greatly improved this work. They would also like to thank Jan Lino Kricke for his support during the mechanical loading analysis of the piezo actuators.

## AUTHOR DECLARATIONS

### Conflict of Interest

The authors have no conflicts to disclose.

### Author Contributions

**F. Eckelt**: Conceptualization (equal); Data curation (lead); Formal analysis (lead); Investigation (lead); Software (lead); Visualization

(equal); Writing – original draft (lead); Writing – review & editing (equal). **I. Cavallaro**: Conceptualization (equal); Resources (equal). **R. Wagner**: Conceptualization (equal); Resources (equal). **A.-A. Haghighirad**: Resources (equal). **T. Wolf**: Resources (equal). **J. Wilmers**: Formal analysis (equal); Investigation (equal); Methodology (equal); Software (equal); Writing – review & editing (equal). **S. Bargmann**: Methodology (equal); Writing – review & editing (equal). **C. Hess**: Conceptualization (equal); Funding acquisition (lead); Supervision (lead); Writing – review & editing (equal).

## DATA AVAILABILITY

The data that support the findings of this study are available from the corresponding author upon reasonable request.

## REFERENCES


[1] C. W. Hicks, D. O. Brodsky, E. A. Yelland, A. S. Gibbs, J. A. N. Bruin, M. E. Barber, S. D. Edkins, K. Nishimura, S. Yonezawa, Y. Maeno, and A. P. Mackenzie, "Strong increase of $t_c$ of $Sr_2RuO_4$ under both tensile and compressive strain," Science **344**, 283–285 (2014).

[2] H. Taniguchi, K. Nishimura, S. K. Goh, S. Yonezawa, and Y. Maeno, "Higher-$t_c$ superconducting phase in $Sr_2RuO_4$ induced by in-plane uniaxial pressure," J. Phys. Soc. Jpn. **84**, 014707 (2015).

[3] H.-H. Kim, S. M. Souliou, M. E. Barber, E. Lefrançois, M. Minola, M. Tortora, R. Heid, N. Nandi, R. A. Borzi, G. Garbarino, A. Bosak, J. Porras, T. Loew, M. König, P. J. W. Moll, A. P. Mackenzie, B. Keimer, C. W. Hicks, and M. Le Tacon, "Uniaxial pressure control of competing orders in a high-temperature superconductor," Science **362**, 1040–1044 (2018).

[4] J.-H. Chu, H.-H. Kuo, J. G. Analytis, and I. R. Fisher, "Divergent nematic susceptibility in an iron arsenide superconductor," Science **337**, 710–712 (2012).

[5] H.-H. Kuo, M. C. Shapiro, S. C. Riggs, and I. R. Fisher, "Measurement of the elastoresistivity coefficients of the underdoped iron arsenide $Ba(Fe_{0.975}Co_{0.025})_2As_2$," Phys. Rev. B **88**, 085113 (2013).

[6] X. Hong, F. Caglieris, R. Kappenberger, S. Wurmehl, S. Aswartham, F. Scaravaggi, P. Lepucki, A. U. B. Wolter, H.-J. Grafe, B. Büchner, and C. Hess, "Evolution of the nematic susceptibility in $LaFe_{1-x}Co_xAsO$," Phys. Rev. Lett. **125**, 067001 (2020).

[7] X. Hong, S. Sykora, F. Caglieris, M. Behnami, I. Morozov, S. Aswartham, V. Grinenko, K. Kihou, C.-H. Lee, B. Büchner, and C. Hess, "Elastoresistivity of heavily hole-doped 122 iron pnictide superconductors," Front. Phys. **10**, 853717 (2022).

[8] P. Wiecki, M. Frachet, A.-A. Haghighirad, T. Wolf, C. Meingast, R. Heid, and A. E. Böhmer, "Emerging symmetric strain response and weakening nematic fluctuations in strongly hole-doped iron-based superconductors," Nat. Commun. **12**, 4824 (2021).

[9] M. S. Ikeda, J. A. W. Straquadine, A. T. Hristov, T. Worasaran, J. C. Palmstrom, M. Sorensen, P. Walmsley, and I. R. Fisher, "AC elastocaloric effect as a probe for thermodynamic signatures of continuous phase transitions," Rev. Sci. Instrum. **90**, 083902 (2019).

[10] Y.-S. Li, M. Garst, J. Schmalian, S. Ghosh, N. Kikugawa, D. A. Sokolov, C. W. Hicks, F. Jerzembeck, M. S. Ikeda, Z. Hu, B. J. Ramshaw, A. W. Rost, M. Nicklas, and A. P. Mackenzie, "Elastocaloric determination of the phase diagram of $Sr_2RuO_4$," Nature **607**, 276–280 (2022).

[11] M. S. Ikeda, T. Worasaran, E. W. Rosenberg, J. C. Palmstrom, S. A. Kivelson, and I. R. Fisher, "Elastocaloric signature of nematic fluctuations," Proc. Natl. Acad. Sci. U. S. A. **118**, e2105911118 (2021).

[12] M. A. Tanatar, E. C. Blomberg, A. Kreyssig, M. G. Kim, N. Ni, A. Thaler, S. L. Bud'ko, P. C. Canfield, A. I. Goldman, I. I. Mazin, and R. Prozorov, "Uniaxial-strain mechanical detwinning of $CaFe_2As_2$ and $BaFe_2As_2$ crystals: Optical and transport study," Phys. Rev. B **81**, 184508 (2010).

[13] C. Dhital, Z. Yamani, W. Tian, J. Zeretsky, A. S. Sefat, Z. Wang, R. J. Birgeneau, and S. D. Wilson, "Effect of uniaxial strain on the structural and magnetic phase transitions in $BaFe_2As_2$," Phys. Rev. Lett. **108**, 087001 (2012).

[14] X. Ren, L. Duan, Y. Hu, J. Li, R. Zhang, H. Luo, P. Dai, and Y. Li, "Nematic crossover in $BaFe_2As_2$ under uniaxial stress," Phys. Rev. Lett. **115**, 197002 (2015).

[15] J.-H. Chu, J. G. Analytis, K. De Greve, P. L. McMahon, Z. Islam, Y. Yamamoto, and I. R. Fisher, "In-plane resistivity anisotropy in an underdoped iron arsenide superconductor," Science **329**, 824–826 (2010).

[16] L. Degiorgi, "Optical fingerprints of nematicity in iron-based superconductors," Front. Phys. **10**, 866664 (2022).

[17] H. J. Conley, B. Wang, J. I. Ziegler, R. F. Haglund, Jr., S. T. Pantelides, and K. I. Bolotin, "Bandgap engineering of strained monolayer and bilayer $MoS_2$," Nano Lett. **13**, 3626–3630 (2013).

[18] T. M. G. Mohiuddin, A. Lombardo, R. R. Nair, A. Bonetti, G. Savini, R. Jalil, N. Bonini, D. M. Basko, C. Galiotis, N. Marzari, K. S. Novoselov, A. K. Geim, and A. C. Ferrari, "Uniaxial strain in graphene by Raman spectroscopy: *G* peak splitting, Grüneisen parameters, and sample orientation," Phys. Rev. B **79**, 205433 (2009).

[19] C. W. Hicks, M. E. Barber, S. D. Edkins, D. O. Brodsky, and A. P. Mackenzie, "Piezoelectric-based apparatus for strain tuning," Rev. Sci. Instrum. **85**, 065003 (2014).

[20] W. Martienssen and H. Warlimont, *Springer Handbook of Condensed Matter and Materials Data: CD-ROM*, *Springer Handbook of Condensed Matter and Materials Data* (Springer, 2005).

[21] HEMPEL metals and more, Titan grade 2–3.7025, UNS R50400, Werkstoff, Material, Metall, 2024, https://www.hempel-metals.de/de/werkstoffe/titanlegierungen/ti-gr-2-37035/ (accessed 20 June 2024).

[22] MicroEpsilon, "capaNCDT, Kapazitive Sensoren für Weg, Abstand und Position," https://www.micro-epsilon.de/fileadmin/download/products/cat–capaNCDT–de.pdf (accessed 26 Nov 2025).

[23] R. M. Fernandes, A. V. Chubukov, and J. Schmalian, "What drives nematic order in iron-based superconductors?," Nat. Phys. **10**, 1745–2481 (2014).

[24] R. M. Fernandes, A. E. Böhmer, C. Meingast, and J. Schmalian, "Scaling between magnetic and lattice fluctuations in iron pnictide superconductors," Phys. Rev. Lett. **111**, 137001 (2013).

[25] P. C. Canfield and S. L. Bud'ko, "FeAs-based superconductivity: A case study of the effects of transition metal doping on $BaFe_2As_2$," Annu. Rev. Condens. Matter Phys. **1**, 27–50 (2010).

[26] H.-H. Kuo, J.-H. Chu, J. C. Palmstrom, S. A. Kivelson, and I. R. Fisher, "Ubiquitous signatures of nematic quantum criticality in optimally doped Fe-based superconductors," Science **352**, 958–962 (2016).